The following publication Zhang, X., Kim, D., Guo, X., Zhu, Y., & Lee, L. Y. S. (2021). Impacts of boron doping on the atomic structure, stability, and photocatalytic activity of Cu3P nanocrystals. Applied Catalysis B: Environmental, 298, 120515 is available at https://doi.org/10.1016/j.apcatb.2021.120515.

Boron Substitution in Cu_3P Nanocrystals: Modification of Atomic Structure and Promotion of Photocatalytic Performance

Xiandi Zhang,[1] *Daekyu Kim,*[1] *Xuyun Guo,*[2] *Ye Zhu,*[2,3] *and Lawrence Yoon Suk Lee*[1,3,]*

[1] Department of Applied Biology and Chemical Technology and the State Key Laboratory of Chemical Biology and Drug Discovery, The Hong Kong Polytechnic University, Hung Hom, Kowloon, Hong Kong SAR, China

[2] Department of Applied Physics, The Hong Kong Polytechnic University, Hung Hom, Kowloon, Hong Kong SAR, China

[3] Research Institute for Smart Energy, The Hong Kong Polytechnic University, Hung Hom, Kowloon, Hong Kong SAR, China

*E-mail: lawrence.ys.lee@polyu.edu.hk (L. Y. S. Lee)

Keywords: boron doping; copper phosphide; hydrogen evolution reaction; photocatalysis; structural modification

Abstract

Heteroatom doping is an effective way to modify the crystal structure of materials and tune their intrinsic properties towards targeted applications. A light element boron (B) has been recognized as a versatile dopant that can replace the atom in the host materials, enabling tuneable catalytic properties. However, the role of B dopant in photocatalytic reactions is still elusive. Herein, we report the preparation of B-doped Cu_3P nanocrystals (B-Cu_3P) that shows an almost four-time promotion of photocatalytic hydrogen evolution reaction (HER) rate compared with the pristine Cu_3P. This improvement is credited to the replacement of P with B atom, which modifies atomic configuration and bonding environments of Cu_3P and endows with enhanced photostability and charge carrier generation. Computational calculations indicate that the boron-associated reconfiguration of electronic structure also improves the conductivity of B-Cu_3P by downshifting the Fermi level, leading to a higher charge density and optimized Gibbs free energy of H adsorption. This work demonstrates the impact and role of B-doping in revamping metal phosphides with improved kinetics and thermodynamics for photocatalytic reactions.

1. Introduction

Transition metal phosphides (TMPs) have recently gained broad interest as active catalysts for energy conversion reactions, such as hydrogen evolution reaction (HER), oxygen reduction reaction (ORR), and methanol oxidation reaction,[1] after being overlooked for over two centuries since the first report.[2] In those important reactions, especially HER, that are vital for realizing renewable and sustainable next-generation energy platform, TMPs offer the advantage of chemical and mechanical durability, electrical conductivity, as well as low cost. The pioneering works on Ni_2P[3] have demonstrated its unique ensemble effect, where the Ni and P sites on the surface act as hydride-acceptor and proton-acceptor centers, respectively,[4] and inspired a number of TMP compounds to be designed as highly active electrocatalysts for H_2 production.[1c, 5] As DFT calculations indicated,[3a] the P atoms on the surface of TMPs endow them with an intrinsic charged character ($M^{\delta+}$ and $P^{\delta-}$) that traps protons during HER process and thus provides high activity for H_2 dissociation. The exploration of TMPs as an HER catalyst is, however, mainly focused on Ni, Co, Fe, Mo-based single metal TPMs[1d, 6] or bimetallic TMPs.[7] Moreover, the application of TMPs in photocatalysis is largely limited by their metallic properties lacking the light absorptivity.

Some TMPs have been proposed as a co-catalyst in composite photocatalytic systems to collect photogenerated electrons from semiconductors such as CdS and g-C_3N_4 and facilitate the transfer of electron.[6a, 6c, 8] Because the loading amount of TMPs in such composites is restrained, usually less than 5 wt.%, in order not to interfere the light absorption of semiconductors, the enhancement of HER performance by TMPs is limited. As an exceptional TMP with a narrow bandgap, Cu_3P nanoparticles deposited on g-C_3N_4 were reported to act as a photocatalyst,[9] but the contribution of Cu_3P to HER performances were not very impressive. It is believed that the intrinsic HER activity of Cu_3P is hampered by unfavorable Gibbs free energy for hydrogen adsorption (ΔG_{H^*}) that is lowered by highly electronegative P atoms far below the optimal value (= 0).[10] Such negative values of ΔG_{H^*} render the desorption of adsorbed hydrogen (H*) to form H_2 difficult, making it a rate-determining step of HER process.[10a, 11] In addition, the high concentration of P atoms in TMPs was reported to weaken the electron delocalization in metal sites, leading to a severely reduced conductivity.[11] It is thus desirable to modulate the electronic structure of Cu_3P to achieve the balance between the rates of H^+ reduction and the removal of H_2

from the surface as well as improved conductivity.

Doping TMPs with a foreign element, either metal or non-metal, can offer a tunable modification of their electronic characters which results in favorable adsorption of intermediates or improved electrical conductivity, thus promoting electrocatalytic HER activities.[10, 12] Our previous study also demonstrated that the incorporation of S atoms into Cu_3P lattice constructed a phosphosulfide structure that enabled photocatalytic H_2 generation without any assistance of co-catalysts,[13] but both activity and stability were unsatisfactory due to the fast recombination of charge carriers and unstable structure. Among various dopants available, boron (B) has been less popular due to the difficulties in experimental approach and its characterization. Nevertheless, it was shown that the incorporation of B can dramatically enhance the catalytic activity[14] and stability of carbon-based electrocatalyst.[15] Recently, Cao *et al.*[5d] demonstrated the B-induced electronic structure reformation of CoP, which afforded an improved pH-universal HER electrocatalyst. The B-doping of photocatalysts also has beneficial effects of promoting the visible-light absorption and catalytic activity,[16] but the fundamental understanding of B-modified structure and its influence on photocatalytic activity are lacking.

Herein, we report a novel B-doped Cu_3P nanocrystals of which P atoms are partially replaced with B atoms. The B-modified Cu_3P structure exhibits highly enhanced stability and photocatalytic activity, demonstrating a nearly four-fold promotion of H_2 production rate compared with the pristine Cu_3P. Various techniques, including *in situ* high-temperature powder X-ray diffraction pattern (PXRD), X-ray photoelectron spectroscopy (XPS), extended X-ray absorption fine structure (EXAFS), and Pawley refinement and pair distribution function (PDF) fitting of high-resolution PXRD, were engaged to unveil the phase evolution of Cu_3P with B doping and its impacts on atomic configuration and bonding environments. The electrochemical studies and computational calculations indicate that the incorporation of B atoms can stabilize the original Cu_3P structure with the enhanced charge density and optimized Gibbs free energy of H adsorption, leading to superior kinetics and thermodynamics for photocatalytic HER performance.

2. Results and Discussions

Boron-doped Cu_3P (B-Cu_3P) was prepared *via* a two-step method as illustrated in **Figure 1a**. Briefly, Cu^{2+} ions are first treated with $NaBH_4$ solution to form boron-doped copper salts (B-

$Cu^{\delta+}$) followed by the coordination with oleylamine (OLA) as a B-Cu–OLA complex.[9a] Further reaction with PH_3 gas that is generated from NaH_2PO_2 converts the B-doped Cu(I)-complex to B-Cu_3P nanocrystals. Based on the $NaBH_4$ concentration used (0.03, 0.05, 0.07, and 0.10 M), the obtained products are denoted as $B_{0.03}$-Cu_3P, $B_{0.05}$-Cu_3P, $B_{0.07}$-Cu_3P, and $B_{0.10}$-Cu_3P, and inductively coupled plasma optical emission spectroscopy (ICP-OES, **Figure S1**) verifies their boron contents as 2.3, 5.3, 2.7, and 1.9 %, respectively.

2.1. Characterizations of Boron-doped Cu_3P Nanoparticles

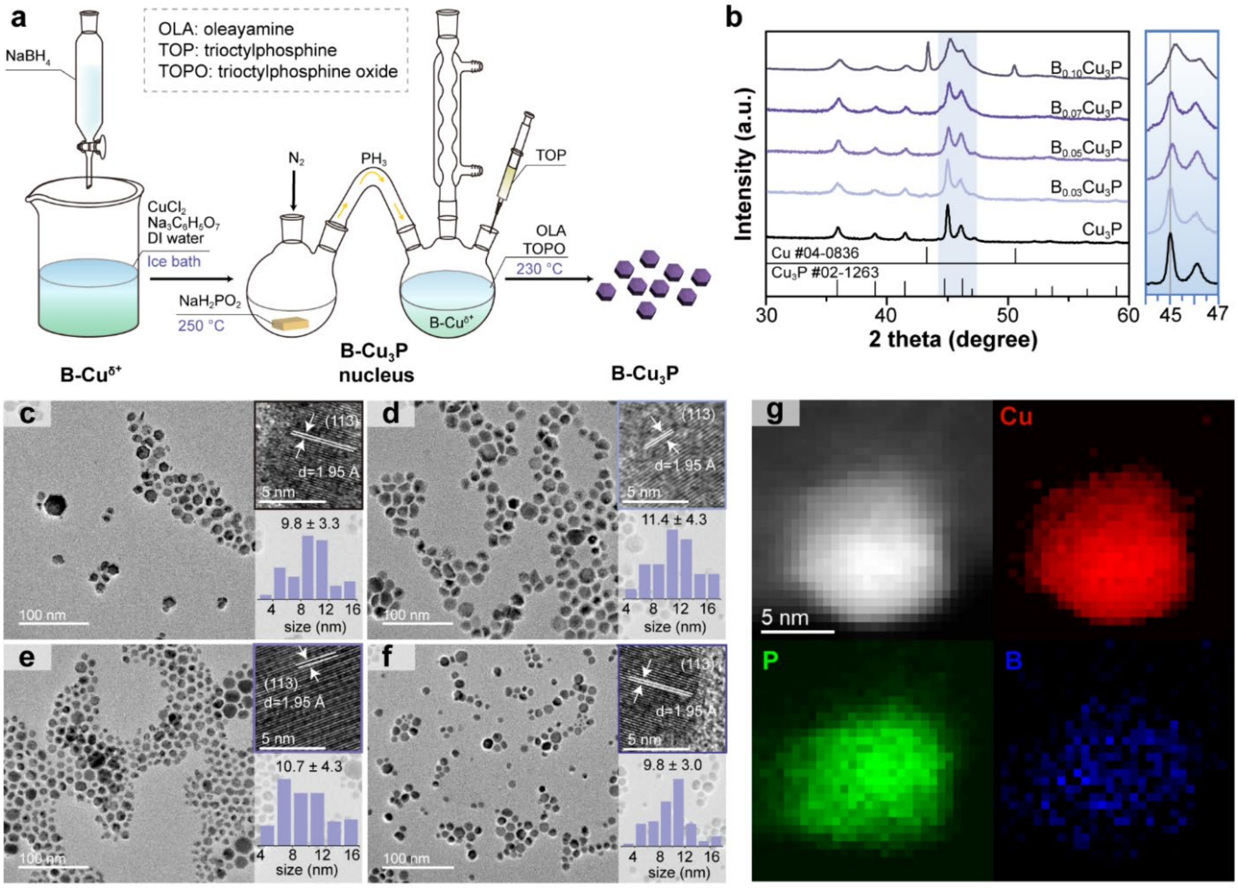

Figure 1. Schematic illustration of the synthetic procedure of B-Cu_3P. (b) PXRD patterns of Cu_3P and B-Cu_3P samples. TEM images of (c) Cu_3P, (d) $B_{0.03}$-Cu_3P, (e) $B_{0.05}$-Cu_3P, and (f) $B_{0.07}$-Cu_3P. Insets are the corresponding HRTEM images and particle size distribution. (g) STEM-EELS maps of $B_{0.05}$-Cu_3P.

The structure and morphology of B-Cu_3P were first examined by powder X-ray diffraction pattern (PXRD) and scanning transmission electron microscopy (STEM). As shown in **Figure 1b**, pristine Cu_3P exhibits diffraction peaks at 36.1°, 39.2°, 41.8°, 45.1°, 46.1°, and 47.3°, which correspond to the (112), (202), (211), (300), (113), and (212) planes of Cu_3P (PDF# 02-1263).[13] Similar diffraction patterns with slight peak broadenings and shifts (*ca.* 1° – 2°) toward higher angles are observed after the B-doping (**Figure 1b**, right), suggesting a possible coordination of boron atoms within the Cu_3P crystal structure. The $B_{0.10}$-Cu_3P of the highest B-doping shows two additional peaks at 43.3° and 50.4°, which are attributed to metallic Cu^0 species (PDF# 04-0836). Based on the results of PXRD and ICP-OES, the maximum amount of boron atoms that can be doped to Cu_3P without forming metallic phase is *ca.* 5.3 % ($B_{0.05}$-Cu_3P). The excessive amount of BH_4^- is believed to fully reduce the B-$Cu^{\delta+}$ precursor to metallic Cu^0.

Figure 1c–1f show the morphologies of Cu_3P and B-Cu_3P samples. All samples display hexagonal or rounded hexagonal nanocrystals with an average diameter of *ca.* 10 nm, which indicates that the morphology and size of the pristine Cu_3P are not significantly altered by the incorporation of boron atoms. The high-resolution TEM (HRTEM) images reveal the unchanged *d*-spacing of 1.95 Å from all samples, which corresponds to the (113) plane of the Cu_3P crystal structure (insets in **Figure 1c–1f**). The electron energy loss spectroscopy (EELS)mapping on $B_{0.05}$-Cu_3P, presented in **Figure 1g**, confirms the co-existence of Cu, P, and B atoms evenly distributed over the entire nanocrystal.

2.2. Atomic Structure of B-Cu_3P

A series of characterization techniques were employed to investigate the local atomic configuration of boron-modified Cu_3P. The $B_{0.05}$-Cu_3P, for its highest B-doping level (5.3 %), was selected as the representative of B-Cu_3P samples, and B-Cu_3P refers to $B_{0.05}$-Cu_3P hereafter unless specified otherwise. The chemical state of B-Cu_3P was first probed by X-ray photoelectron spectroscopy (XPS). The XPS survey spectrum shown in **Figure S2** confirms the existence of Cu, P, and B elements in B-Cu_3P. In the Cu 2p region of high-resolution XPS spectra (**Figure 2a**), both Cu_3P and B-Cu_3P display a pair of peaks located at 935.1 and 955.2 eV, which can be attributed to the surface oxidation of Cu_3P.[7] The Cu_3P shows another set of Cu $2p_{3/2}$ and $2p_{1/2}$ peaks at 932.9 and 952.7 eV, respectively, assigned to the Cu^+ species from Cu–P bond,[7] which are negatively shifted by 0.2 eV in the B-Cu_3P. Meanwhile, an opposite shift is evident in the P 2p XPS spectra of B-Cu_3P (**Figure 2b**). The pristine Cu_3P shows a pair of characteristic P $2p_{3/2}$ and $2p_{1/2}$ peaks at 128.8 and 129.8 eV, respectively, which correspond to the P^{3-} species of Cu-P bonds.[17] These P 2p peaks in B-Cu_3P appear at 0.2 eV-higher binding energies, indicating an electron redistribution between Cu and P atoms caused by B-doping.[5d] Another peak at 133.5 eV that arises from surface oxygen species (P–O) is observed from both Cu_3P and B-Cu_3P, which is typical for transition metal phosphides.[18] The high-resolution B 1s spectrum of B-Cu_3P (**Figure 2c**) confirms the formation of Cu–B bond with two peaks at 186.7 and 190.4 eV, which are consistent with the previous reports of metal–B bond and surface oxidized B (B–O), respectively.[5d, 19]

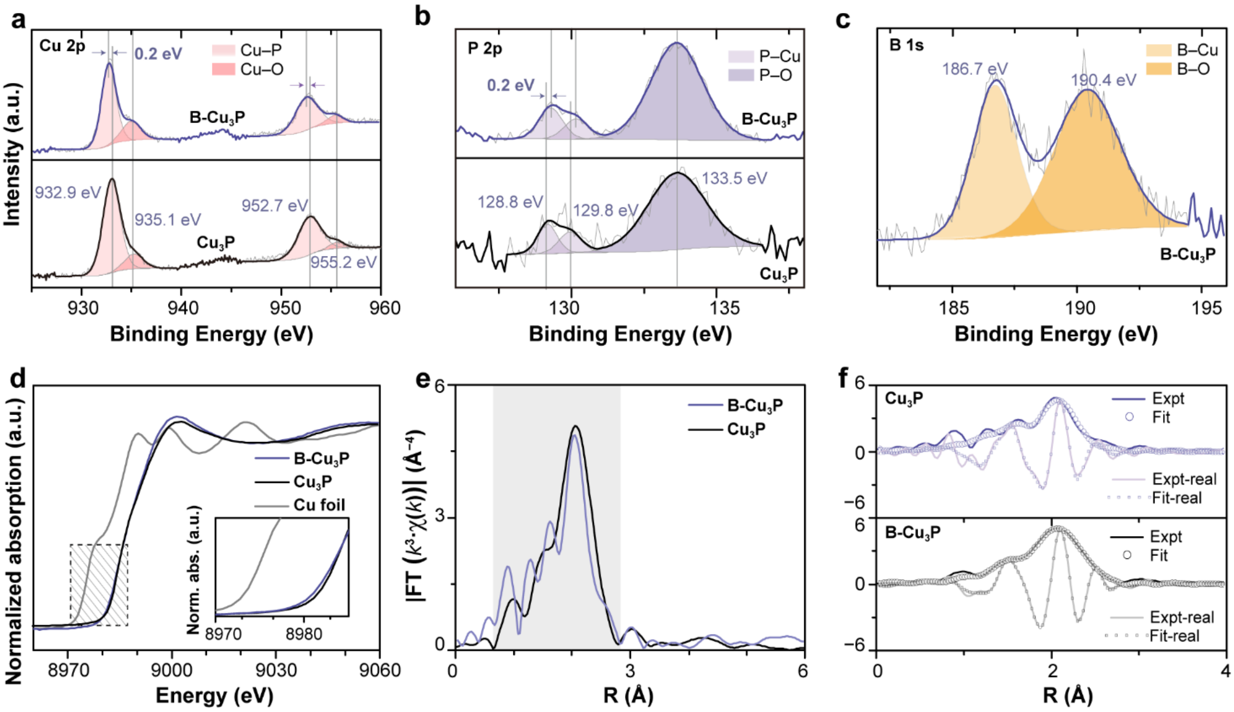

Figure 2. High-resolution XPS spectra of Cu_3P and B-Cu_3P in (a) Cu 2p, (b) P 2p, and (c) B 1s regions. (d) XANES spectra measured at Cu *K*-edge of Cu foil, Cu_3P, and B-Cu_3P. (e) Fourier transformed k^3-weighted EXAFS of Cu_3P and B-Cu_3P and (f) the corresponding fitting results.

X-ray absorption fine structure (XAFS) at Cu *K*-edge was examined to further understand the local coordination environment in B-Cu_3P. In the X-ray absorption near edge structure (XANES, **Figure 2d**), the absorption edge energy of Cu *K*-edge in B-Cu_3P, consistent with the Cu 2p XPS spectrum, slightly shifts to a lower energy compared with that in Cu_3P (**Figure 2a**). This negative shift of absorption edge is most possibly caused by the lower electronegativity of B atom relative to P atom and the structural distortion caused by B incorporation.[5d] The Fourier transformed k^3-weighted extended X-ray absorption fine structure (EXAFS) spectrum of Cu_3P **(Figure 2e)** exhibits three peaks in the distance range between 0.8 and 2.8 Å, suggesting three scattering paths of Cu–P bond. In the spectrum of B-Cu_3P, on the other hand, four peaks are evident in the same distance range, indicating another alternative scattering path of Cu–B bond. Further analyses on the fittings of Fourier transformed EXAFS confirm the Cu–B coordination in B-Cu_3P as illustrated in **Figure 2f** and **Table S1**. The B-Cu_3P exhibits the Cu–B coordination number of 1.0(6) and the reduced Cu–P coordination numbers compared with those in Cu_3P, which can be ascribed to the substitution of P by B atoms.

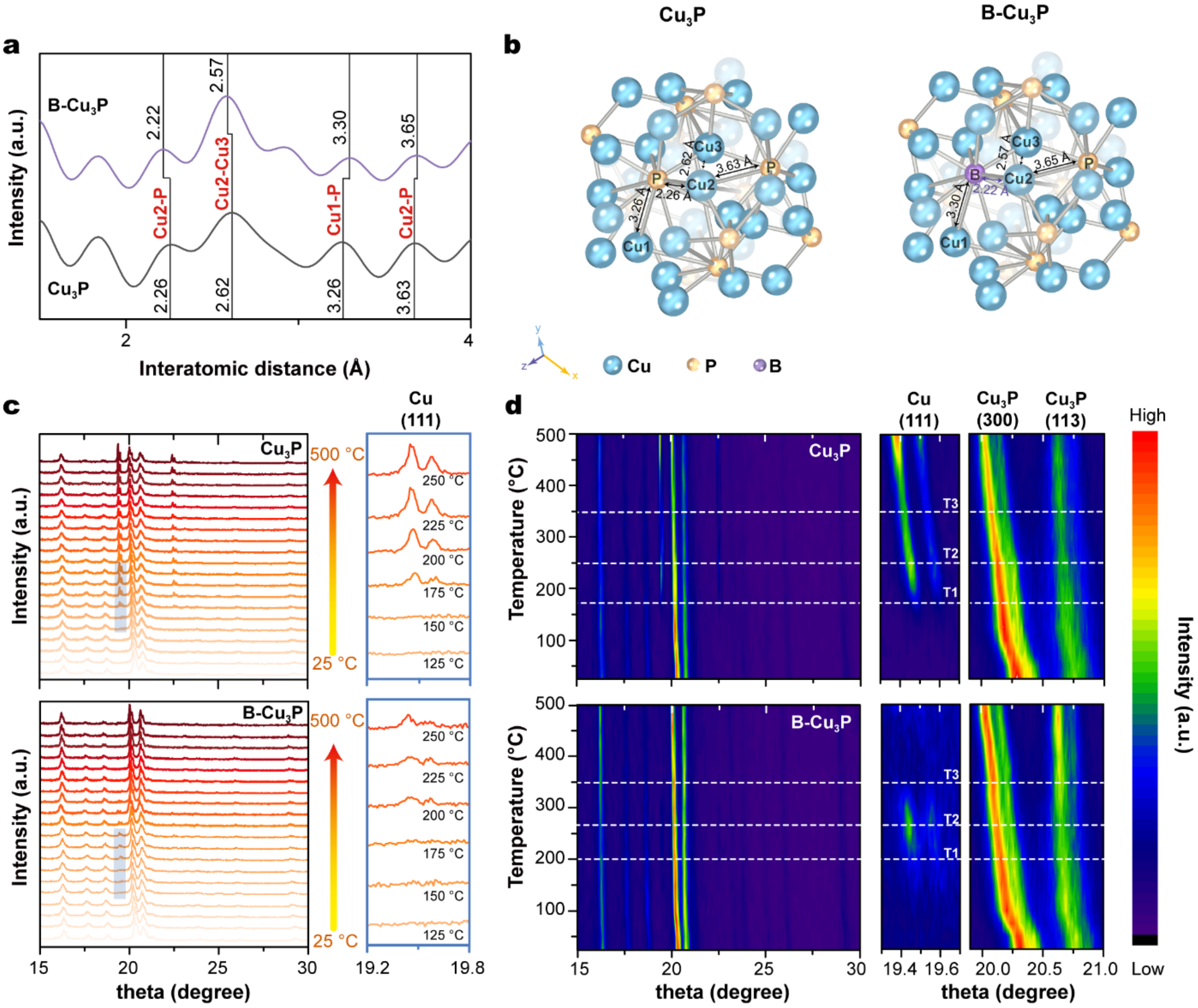

Figure 3. (a) Atomic distances analyzed by PDF fitting, (b) simulated atomic configurations, (c) *in situ* PXRD measured in the temperature range of 25 to 500°, and (d) the corresponding temperature map of Cu_3P and B-Cu_3P. PXRD was conducted under Mo Kα and Kβ radiation with $\lambda = 0.709317$ Å.

To further elucidate the specific position of B substitution in the Cu_3P, Pawley refinement and pair distribution function (PDF) fitting with high-resolution PXRD of Cu_3P and B-Cu_3P were carried out. Based on the refinement results (**Figure S4** and **Table S2**), the cell volume of Cu_3P is calculated as 298.94 Å^3, which is decreased to 296.72 Å^3 in B-Cu_3P, supporting the replacement of P by B atoms of a smaller radius.[5d] The crystal model of PDF fittings is set based on the crystallographic data of Cu_3P (trigonal, $P\bar{3}c1$),[20] where three Cu^+ sites (Cu1, Cu2, and Cu3) are connected with one P^{3-} site (**Figure S5a**). The coordinates and bonding environments of Cu and P atoms in the first coordination shell are shown in **Table S3**. The PDF fittings presented in

Figure S5b suggest the statistic result of distances between an atom to its nearest neighbors.[21] Considering the atomic distances calculated for the first coordination shells of Cu_3P and B-Cu_3P (**Figure 3a** and **Table S4**), the Cu2–P bond receives a direct influence of the B substitution as witnessed by the shortened bond length from 2.26 Å in Cu_3P to 2.22 Å in B-Cu_3P. This change in Cu2–P bond length inevitably results in the distortion of crystal structure. The distance between Cu2 and Cu3 is shortened by 0.05 Å, while the bond lengths of the nearest Cu1–P and the second nearest Cu2–P are increased by 0.04 and 0.02 Å, respectively. The simulation of atomic configurations in B-Cu_3P corroborates these changes in Cu_3P structure induced by B-doping (**Figure 3b**).

In situ high-temperature XRD was employed to have further insights into the B-Cu_3P structure by investigating its phase evolution as temperature rises. The XRD patterns of Cu_3P (**Figure 3c**, top) indicate that a new pair of peaks appears at 19.5° and 19.6° when temperature reaches 175 °C, which is assigned to the (111) plane of metallic Cu phase under Mo Kα and Kβ radiations, and gradually intensifies with the escalation of temperature, suggesting that metallic Cu^0 species is first formed in the early stage of phase transition. The corresponding continuous interpolated images (**Figure 3d**, top) clearly visualize that the thermal expansion of Cu_3P structure causes all diffraction peaks to shift toward lower θ values.[22] The Cu^0 (111) peak evolves with the heating temperature in three discrete stages. In the temperature range of 175 – 250 °C (T1), the Cu^0 (111) peak first emerges and intensifies as seen in the PXRD spectra. The intensity of the Cu^0 (111) peak is gradually reduced from 250 °C until 350 °C (T2) and enhanced again to show the maximum intensity at 500 °C (T3: 350 – 500 °C). Another two peaks in 20.0 – 21.0° θ, corresponding to the (300) and (113) facets of Cu_3P, exhibits an opposite behavior. The intensities of these peaks progressively weaken in the T1 region. After a brief uphold or slight regain in the T2 region, the Cu_3P (300) and (113) peaks continue to diminish in the T3 region. Such complementary variation of Cu^0 and Cu_3P peak intensities suggests that the phase transition of Cu_3P is not a monotonous transformation to metallic Cu^0. Under unstable conditions caused by thermal energy, the Cu–P bonds in Cu_3P start to break and Cu ions are partially removed from the crystal structure and reduced to metallic Cu^0 species, creating a large amount of Cu vacancies.[23] During this phase transition, some of the Cu atoms in Cu^0 phase are believed to bond with P atoms again to form Cu_3P phase (T2 region), but eventually decompose to Cu^0 phase when the temperature is further increased.

With the incorporation of boron, however, the phase transition of B-Cu_3P proceeds in a different way as presented in **Figure 3c** and **3d** (bottom panels). Compared with the pristine Cu_3P, the appearance of metallic Cu^0 phase in B-Cu_3P is slightly retarded to 200 °C. The Cu^0 (111) peak shows the highest intensity at 250 °C (T1: 200 – 250 °C) and quickly shrinks to almost disappear at *ca*. 300 °C in the T2 region. Meanwhile, the Cu_3P (300) and (113) peaks are gradually reduced in the T1 region but retain their intensities until 300 °C of the T2 region. These peaks intensify again at higher temperatures, *i.e.*, T3 region, which implies the reconstruction of Cu_3P from the metallic Cu^0. The Cu_3P peaks, especially the (113) peak, exhibit reduced intensities at the end of the T3 region (480 – 500 °C), suggesting the final decomposition of Cu_3P phase at the higher temperature. This observation of unexpected phase evolutions induced by thermal energy indicates that the incorporation of B atoms stabilizes the Cu_3P phase, which would enhance the durability for its photocatalytic applications.

2.3. Photocatalytic Performances

Figure 4a compares the photocatalytic hydrogen evolution reaction (HER) rates of the as-prepared B-Cu_3P samples with those of the pristine Cu_3P and commercial Degussa TiO_2 P-25 (P25). In a continuous 3-h reaction using catalyst concentration of 50 mg L^{-1}, the Cu_3P records a low HER rate of 0.27 mmol g^{-1} h^{-1}. With the increasing B-doping level, the HER rate of B-Cu_3P is accordingly promoted to reach the maximum rate of 1.04 mmol g^{-1} h^{-1} with the $B_{0.05}$-Cu_3P, which outperforms the commercial P25 (0.36 mmol g^{-1} h^{-1}). The $B_{0.07}$-Cu_3P and $B_{0.10}$-Cu_3P exhibit decreased HER activities compared with the $B_{0.05}$-Cu_3P, which echoes the trend of B-doping levels in the B-Cu_3P samples (**Figure S1**). The exact same trend is observed when an increased amount (100 mg L^{-1}) of catalysts are used.

The stability of catalysts in a long-term photoreduction was also examined as shown in **Figure 4b**. In a continuous 35-h photocatalysis, the pristine Cu_3P starts to lose its activity after *ca*. 21 h and shows a 43.9 % drop of its initial photoactivity at the end, whereas the $B_{0.05}$-Cu_3P maintains the initial HER rate for entire 32 h with a slight 8.8% drop at 35th hour, demonstrating its enhanced durability against photocorrosion. This stability difference of the two samples agrees well with the *in situ* high-temperature XRD results. The crystal structure and morphology of $B_{0.05}$-Cu_3P determined by PXRD and TEM characterizations after the photoreduction supports its enhanced stability (**Figure S6**). The post-HER PXRD pattern of B-Cu_3P remains unchanged with only slight peak broadening. The TEM image after the reaction displays the $B_{0.05}$-Cu_3P nanocrystals of rounded edges, yet, with the same *d*-spacing, confirming its unaltered structure.

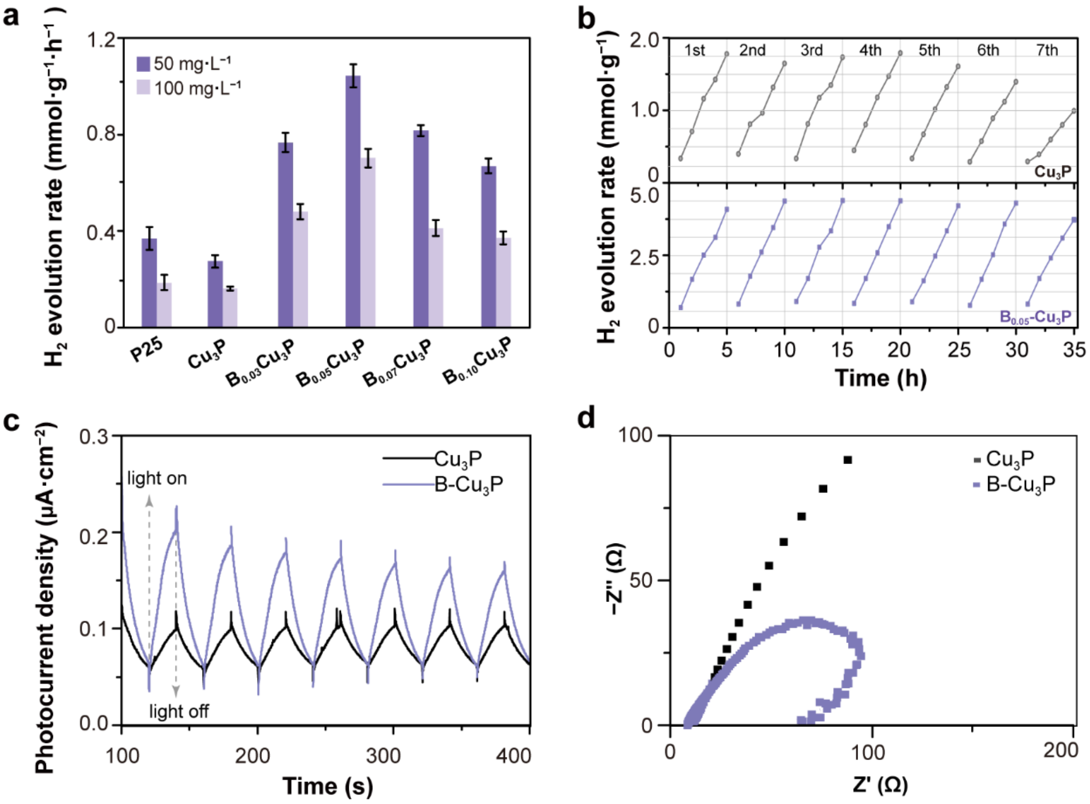

Figure 4. (a) Photocatalytic HER rates of P-25, Cu_3P, and B-Cu_3P samples under the irradiation of 150 W-solar simulator (intensity: 100 mW m^{-2}). (b) Photocatalytic HER rates of Cu_3P and $B_{0.05}$-Cu_3P in a continuous 35-h reaction. (c) Photocurrent measurements and (d) EIS curves of Cu_3P and B-Cu_3P.

2.4. Photocatalytic Mechanism

The B-doping of Cu_3P significantly promoted the stability and photocatalytic HER activity of the resultant B-Cu_3P. To understand the mechanism of such improved photocatalytic performance of B-Cu_3P, the kinetics of reaction was studied by collecting transient photocurrent responses. **Figure 4c** compares the linear sweep voltammograms (LSVs) obtained from Cu_3P and B-Cu_3P using a standard three-electrode system. Compared with the pristine Cu_3P, the B-Cu_3P exhibits a large enhancement in photocurrent density upon the illumination, suggesting a better ability to generate charge carriers and prevent their recombination.[24] Electrochemical impedance spectra (EIS, **Figure 4d**) indicate that the Nyquist arc radius of the B-Cu_3P is substantially reduced, implying a lowered charge transfer resistance by B doping.[5d, 25] The B doping seems to be effective in improving both photogeneration and migration of charge carriers, both of which can lead to the enhanced reaction kinetics of B-Cu_3P.

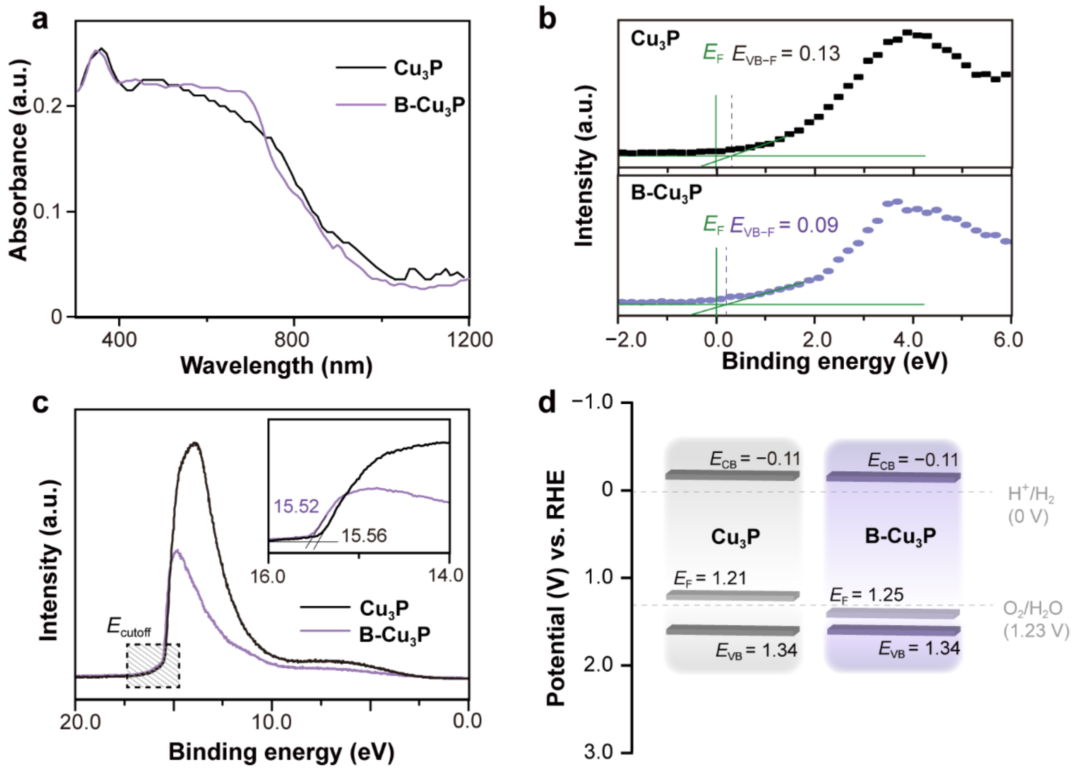

Figure 5. (a) UV–vis–NIR DRS, (b) VB-XPS, and (c) UPS spectra of Cu_3P and B-Cu_3P. (d) Schematic band energy diagrams illustrating the electronic structures of Cu_3P and B-Cu_3P.

Incorporating foreign atoms of dissimilar size can induce structural modifications to the hosting semiconductors due to the distortion or mismatch of lattice alignment. This change in the atomic structure usually accompanies the tuning of electronic configuration, which is important for understanding and directing altered catalytic properties. To establish the relationship between the B-induced modified structure of B-Cu_3P and its enhanced photocatalytic activity, the effect of B doping on the electronic band structure of Cu_3P was investigated by UV–vis–NIR diffuse reflectance spectra (DRS), valence band XPS spectra (VB-XPS), and ultraviolet photoelectron spectra (UPS). A similar absorption edge of *ca*. 860 nm is observed from the UV–vis–NIR DRS of Cu_3P and B-Cu_3P (**Figure 5a**), and the corresponding Tauc plots indicate a band gap of 1.45 eV (**Figure S7**).[26] VB-XPS spectra shown in **Figure 5b** indicate that the energy difference between the Femi level and valence band maximum ($E_{\mathrm{VB\text{-}F}}$) in B-Cu_3P is 0.09 eV, which is decreased from 0.13 eV in Cu_3P. Based on the beginning of secondary photoemission (E_{cutoff}) in UPS spectra (**Figure 5c**), the work function (Φ) of Cu_3P is estimated as 5.65 eV (*vs.* vacuum) using Equation (1).[27] The B-Cu_3P has a slightly increased Φ of 5.69 eV. Thus, the Fermi levels of Cu_3P and B-Cu_3P are calculated as 1.21 and 1.25 eV against reversible hydrogen electrode (RHE), respectively, according to Equation (2). Combining the results from UPS and VB-XPS, the positions of valence band maximum (E_{VB}) and conduction band minimum (E_{CB}) are estimated to be 1.34 and −0.11 eV, respectively, for both Cu_3P and B-Cu_3P, based on Equation (3).

$$hv\ (\mathrm{He},\ 21.21\ \mathrm{eV}) = E_{\mathrm{cutoff}} + \Phi \tag{1}$$

$$E\ (vs.\ \mathrm{RHE}) = -4.44 - E\ (vs.\ \mathrm{vacuum\ level}) \tag{2}$$

$$E_{\mathrm{CB}} = E_{\mathrm{VB}} - E_{\mathrm{g}} \tag{3}$$

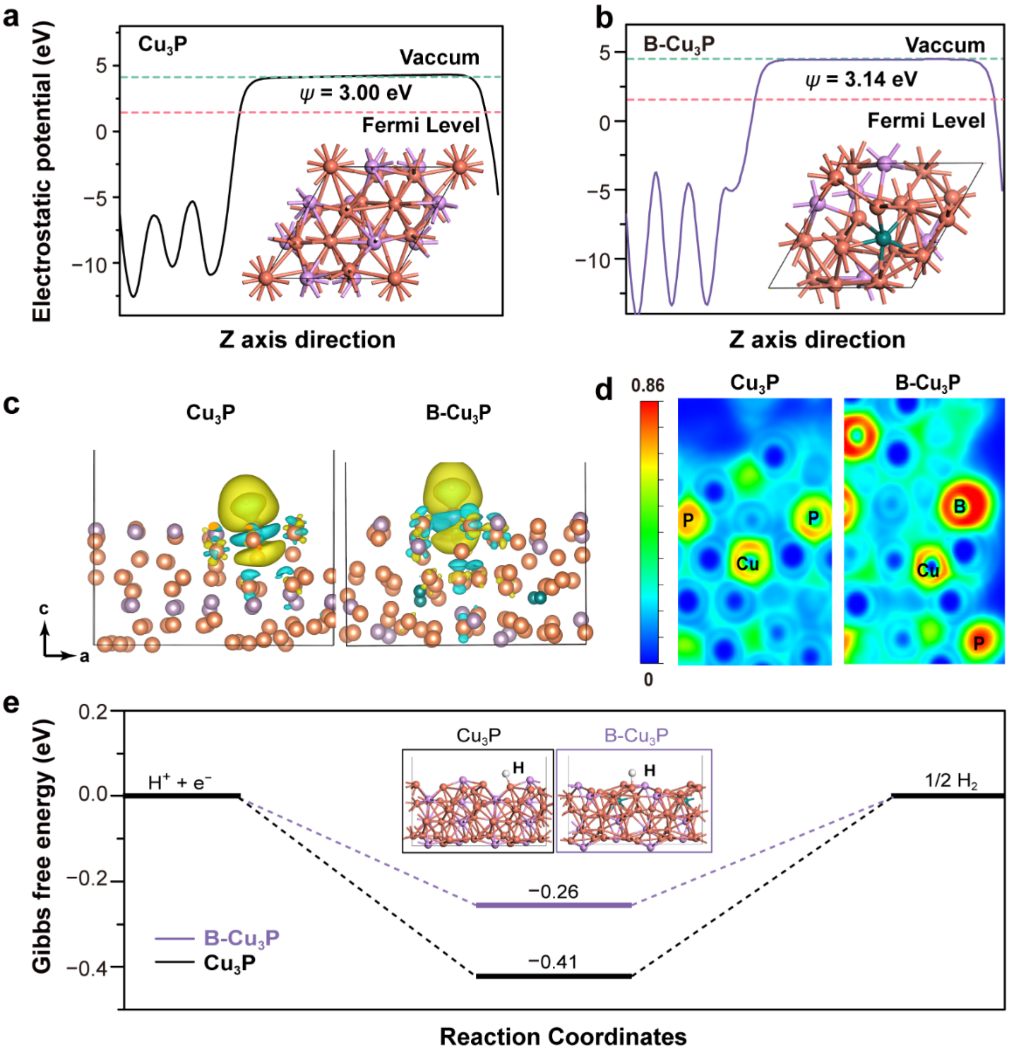

Figure 6. The calculated crystal structure and work functions of (a) Cu_3P and (b) B-Cu_3P. (c) Charge difference of hydrogen adsorbed on Cu_3P and B-Cu_3P. Yellow and cyan areas indicate charge accumulation and depletion, respectively. (d) Electronic location function (ELF) and (e) Gibbs free energy (ΔG_{H^*}) diagram for hydrogen adsorption on Cu_3P and B-Cu_3P. Insets are the most stable atomic configurations of hydrogen adsorption on Cu_3P and B-Cu_3P.

Figure 5d is a schematic band energy diagram illustrating the proposed band structures of Cu_3P and B-Cu_3P, which are typical band structures of p-type semiconductor.[9a] The introduction of B, as an acceptor impurity, has no obvious impact on the positions of VB and CB in this case, but shifts the Fermi level closer to VB. Such a shift of the Fermi level leads to an enhanced carrier concentration and a better conductivity, which is consistent with the results of photocurrent measurement and EIS, and this could be one of the reasons for the promotion of photocatalytic activity.[14a]

Density functional theory (DFT) calculations were employed to further understand the catalytic reaction with B-modified Cu_3P structure. The atomic configurations of Cu_3P and B-Cu_3P were set based on the results of PXRD refinements and PDF fittings (insets in **Figure 6a** and **6b**). The calculated work function of Cu_3P is 3.00 eV and it is increased to 3.14 eV after B doping, a result that is consistent with the result of UPS (**Figure 3c**). The increased work function results in the downshift of the Fermi level closer to the VB, confirming the promoted carrier concentration in B-Cu_3P. The charge density difference was calculated to investigate the charge transfer at the hydrogen adsorbed on B-Cu_3P (**Figure 6c**), and the results suggest that more electrons accumulate around H atoms after B doping, indicating an accelerated charge transfer.[28] In the result of electronic location function (ELF, **Figure 6d**), the substitutional B in B-Cu_3P obviously induces the charge localization around P atoms in the vicinity compared with that of Cu_3P, which increases the charge density in B-Cu_3P and thus favors the H adsorption in the catalytic reaction.[29] This conclusion is also confirmed by Gibbs free energy for H adsorption (ΔG_{H*}) diagram (**Figure 6e**). The ΔG_{H*} is changed from −0.41 eV in Cu_3P to −0.26 eV in B-Cu_3P, which is located closer to 0 eV with B introduction, suggesting that the new structure of B-Cu_3P is thermodynamically more favorable toward photocatalytic HER than Cu_3P.

3. Conclusion

In summary, a boron-modified Cu_3P nanoparticle was prepared in this work. Various techniques were used to reveal the new structure of B-Cu_3P on the atomic level including the bond distance changes around the inserted B atoms. *In situ* high-temperature PXRD indicate that the incorporation of B atoms in Cu_3P results in a more stable atomic configuration, increasing its structural durability. The electronic structure of Cu_3P is also modified by B-doping to promote the charge density and facilitate the charge transfer at the hydrogen adsorbed on B-Cu_3P, leading to an optimized Gibbs free energy for H adsorption and thereby enhancing photocatalytic performance. This work provides useful information that correlates the modification of atomic structure by doping a light element boron with the enhancement in photocatalytic performances and guides the design of other photocatalysts.

Acknowledgement

We gratefully acknowledge the financial supports from the Innovation and Technology Commission of Hong Kong and The Hong Kong Polytechnic University (1-BE0Y).

Supporting Information

An online version of Supplementary data including Experimental, ICP-OES spectra, parameters of PXRD refinement, PDF, and EXAFS fitting, XPS survey spectra, Tauc plots associated with this article is available.

Conflict of Interest

The authors declare no conflict of interest.

Reference

[1] a) P. Xiao, W. Chen, X. Wang, *Adv. Energy Mater.* **2015**, *5*, 1500985; b) Y. Shi, B. Zhang, *Chem. Soc. Rev.* **2016**, *45*, 1529-1541; c) A. Kondori, M. Esmaeilirad, A. Baskin, B. Song, J. Wei, W. Chen, C. U. Segre, R. Shahbazian-Yassar, D. Prendergast, M. Asadi, *Adv. Energy Mater.* **2019**, *9*, 1900516; d) X. Wang, Y. V. Kolen'ko, X. Q. Bao, K. Kovnir, L. Liu, *Angew. Chem. Int. Ed.* **2015**, *54*, 8188-8192; e) J. Xu, Y. Liu, J. Li, I. Amorim, B. Zhang, D. Xiong, N. Zhang, S. M. Thalluri, J. P. S. Sousa, L. Liu, *J. Mater. Chem. A* **2018**, *6*, 20646-20652; f) P. He, X. Y. Yu, X. W. Lou, *Angew. Chem. Int. Ed.* **2017**, *56*, 3897-3900.

[2] B. Pelletier, C. Pelletier, J. Sédillot, *Mémoires et Observations de Chimie, Vol. 2*, Chez Croullerois, Paris, **1798**.

[3] a) P. Liu, J. A. Rodriguez, *J. Am. Chem. Soc.* **2005**, *127*, 14871-14878; b) E. J. Popczun, J. R. McKone, C. G. Read, A. J. Biacchi, A. M. Wiltrout, N. S. Lewis, R. E. Schaak, *J. Am. Chem. Soc.* **2013**, *135*, 9267-9270.

[4] J. Tian, Q. Liu, A. M. Asiri, X. Sun, *J. Am. Chem. Soc.* **2014**, *136*, 7587-7590.

[5] a) Z. Fang, L. Peng, Y. Qian, X. Zhang, Y. Xie, J. J. Cha, G. Yu, *J. Am. Chem. Soc.* **2018**, *140*, 5241-5247; b) I. K. Mishra, H. Zhou, J. Sun, F. Qin, K. Dahal, J. Bao, S. Chen, Z. Ren, *Energy Environ. Sci.* **2018**, *11*, 2246-2252; c) X. Zhang, X. Yu, L. Zhang, F. Zhou, Y. Liang, R. Wang, *Adv. Funct. Mater.* **2018**, *28*, 1706523; d) E. Cao, Z. Chen, H. Wu, P. Yu, Y. Wang, F. Xiao, S. Chen, S. Du, Y. Xie, Y. Wu, Z. Ren, *Angew. Chem. Int. Ed.* **2020**, *59*, 4154-4160.

[6] a) W. Wang, T. An, G. Li, D. Xia, H. Zhao, J. C. Yu, P. K. Wong, *Appl. Catal. B Environ.* **2017**, *217*, 570-580; b) Y. Huang, J. Ge, J. Hu, J. Zhang, J. Hao, Y. Wei, *Adv. Energy Mater.* **2018**, *8*, 1701601; c) D. Zeng, T. Zhou, W. Ong, M. Wu, X. Duan, W. Xu, Y. Chen, Y. Zhu, D. Peng, *ACS Appl. Mater. Interfaces* **2019**, *11*, 5651-5660; d) H. Li, P. Wen, D. S. Itanze, M. W. Kim, S. Adhikari, C. Lu, L. Jiang, Y. Qiu, S. M. Geyer, *Adv. Mater.* **2019**, *31*, e1900813.

[7] X. Jin, J. Li, Y. Cui, X. Liu, X. Zhang, J. Yao, B. Liu, *Inorg. Chem.* **2019**, *58*, 11630-11635.

[8] a) P. Wang, S. Zhan, H. Wang, Y. Xia, Q. Hou, Q. Zhou, Y. Li, R. R. Kumar, *Appl. Catal. B Environ.* **2018**, *230*, 210-219; b) S. Cao, Y. Chen, C.-C. Hou, X.-J. Lv, W.-F. Fu, *J. Mater. Chem. A* **2015**, *3*, 6096-6101.

[9] a) G. Manna, R. Bose, N. Pradhan, *Angew. Chemie.* **2013**, *125*, 6894-6898; b) W. Wang, X. Zhao, Y. Cao, Z. Yan, R. Zhu, Y. Tao, X. Chen, D. Zhang, G. Li, D. Phillips, *ACS Appl. Mater.*

Interfaces **2019**, *11*, 16527-16537; c) R. Shen, J. Xie, X. Lu, X. Chen, X. Li, *ACS Sustainable Chem. Eng.* **2018**, *6*, 4026-4036.

[10] a) Q. Zhou, Z. Shen, C. Zhu, J. Li, Z. Ding, P. Wang, F. Pan, Z. Zhang, H. Ma, S. Wang, H. Zhang, *Adv. Mater.* **2018**, *30*, 1800140; b) H. Tabassum, W. Guo, W. Meng, A. Mahmood, R. Zhao, Q. Wang, R. Zou, *Adv. Energy Mater.* **2017**, *7*, 1601671.

[11] Y. Zheng, Y. Jiao, L. H. Li, T. Xing, Y. Chen, M. Jaroniec, S. Z. Qiao, *ACS Nano* **2014**, *8*, 5290-5296.

[12] a) J. Kibsgaard, T. F. Jaramillo, *Angew. Chem. Int. Ed.* **2014**, *53*, 14433-14437; b) J. Zhuo, M. Cabán-Acevedo, H. Liang, L. Samad, Q. Ding, Y. Fu, M. Li, S. Jin, *ACS Catal.* **2015**, *5*, 6355-6361; c) H.-W. Man, C.-S. Tsang, M. M.-J. Li, J. Mo, B. Huang, L. Y. S. Lee, Y.-C. Leung, K.-Y. Wong, S. C. E. Tsang, *Chem. Commun.* **2018**, *54*, 8630-8633; d) H.-W. Man, C.-S. Tsang, M. M.-J. Li, J. Mo, B. Huang, L. Y. S. Lee, Y.-C. Leung, K.-Y. Wong, S. C. E. Tsang, *Appl. Catal. B Environ.* **2019**, *242*, 186-193; e) M. Liu, Q. He, S. Huang, W. Zou, J. Cong, X. Xiao, P. Li, J. Cai, L. Hou, *ACS Appl. Mater. Interfaces* **2021**, *13*, 9932-9941.

[13] X. Zhang, K.-A. Min, W. Zheng, J. Hwang, B. Han, L. Y. S. Lee, *Appl. Catal. B Environ.* **2020**, *273*, 118927.

[14] a) X. Li, L. Fan, Z. Li, K. Wang, M. Zhong, J. Wei, D. Wu, H. Zhu, *Adv. Energy Mater.* **2012**, *2*, 425-429; b) X. Yu, P. Han, Z. Wei, L. Huang, Z. Gu, S. Peng, J. Ma, G. Zheng, *Joule* **2018**, *2*, 1610-1622.

[15] L. Yang, S. Jiang, Y. Zhao, L. Zhu, S. Chen, X. Wang, Q. Wu, J. Ma, Y. Ma, Z. Hu, *Angew. Chem. Int. Ed.* **2011**, *50*, 7132-7135.

[16] a) A. Zaleska, E. Grabowska, J. W. Sobczak, M. Gazda, J. Hupka, *Appl. Catal. B Environ.* **2009**, *89*, 469-475; b) S. In, A. Orlov, R. Berg, F. Garcı´a, S. Pedrosa-Jimenez, M. S. Tikhov, D. S. Wright, R. M. Lambert, *J. Am. Chem. Soc.* **2007**, *129*, 13790-13791; c) D. Kim, K. Yong, *Appl. Catal. B Environ.* **2021**, *282*, 119538; d) D. Zhao, Y. Wang, C.-L. Dong, Y.-C. Huang, J. Chen, F. Xue, S. Shen, L. Guo, *Nat. Energy* **2021**.

[17] S. Hua, D. Qu, L. An, W. Jiang, Y. Wen, X. Wang, Z. Sun, *Appl. Catal. B Environ.* **2019**, *240*, 253-261.

[18] X. Zhang, J. Yan, L. Y. S. Lee, *Appl. Catal. B Environ.* **2021**, *283*, 119624.

[19] D. J. Joyner, O. Johnson, D. M. Hercules, *J. Am. Chem. Soc.* **2002**, *102*, 1910-1917.

[20] B. Steenberg, *The Crystal Structure of Cu$_3$As and Cu$_3$P, Vol. 12*, Stockholm Almqvist & Wiksell Berlin Friedländer, USW, **1938**.

[21] U. P. Gawai, D. K. Gaikwad, M. R. Bodke, H. A. Khawal, K. K. Pandey, A. K. Yadav, S. N. Jha, D. Bhattacharyya, B. N. Dole, *Phys. Chem. Chem. Phys.* **2019**, *21*, 1294-1307.

[22] X. J. Xu, G. T. Fei, W. H. Yu, L. Chen, L. De Zhang, X. Ju, X. P. Hao, B. Y. Wang, *Appl. Phys. Lett.* **2006**, *88*, 211902.

[23] A. Wolff, T. Doert, J. Hunger, M. Kaiser, J. Pallmann, R. Reinhold, S. Yogendra, L. Giebeler, J. Sichelschmidt, W. Schnelle, R. Whiteside, H. Q. N. Gunaratne, P. Nockemann, J. J. Weigand, E. Brunner, M. Ruck, *Chem. Mater.* **2018**, *30*, 7111-7123.

[24] Y. Chen, S. Ji, W. Sun, Y. Lei, Q. Wang, A. Li, W. Chen, G. Zhou, Z. Zhang, Y. Wang, L. Zheng, Q. Zhang, L. Gu, X. Han, D. Wang, Y. Li, *Angew. Chem. Int. Ed.* **2020**, *59*, 1295-1301.

[25] G. Zuo, Y. Wang, W. L. Teo, A. Xie, Y. Guo, Y. Dai, W. Zhou, D. Jana, Q. Xian, W. Dong, Y. Zhao, *Angew. Chem. Int. Ed.* **2020**, *59*, 11287-11292.

[26] X. Yue, S. Yi, R. Wang, Z. Zhang, S. Qiu, *Nanoscale* **2016**, *8*, 17516-17523.

[27] F. Liu, R. Shi, Z. Wang, Y. Weng, C. M. Che, Y. Chen, *Angew. Chem. Int. Ed.* **2019**, *58*, 11791-11795.

[28] J. Li, X. a. Dong, Y. Sun, W. Cen, F. Dong, *Appl. Catal. B Environ.* **2018**, *226*, 269-277.

[29] a) J. Fu, K. Liu, K. Jiang, H. Li, P. An, W. Li, N. Zhang, H. Li, X. Xu, H. Zhou, D. Tang, X. Wang, X. Qiu, M. Liu, *Adv. Sci.* **2019**, *6*, 1900796; b) C. Pan, Y. Chen, N. Wu, M. Zhang, L. Yuan, C. Zhang, *Materials* **2017**, *10*.